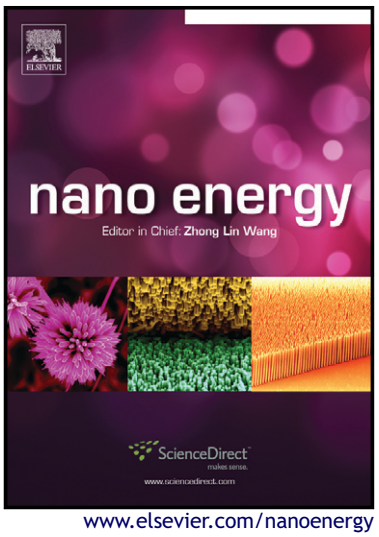

www.elsevier.com/nanoenergy

Transition metal oxides for high performance sodium ion battery anodes

Yinzhu Jiang, Meijuan Hu, Dan Zhang, Tianzhi Yuan, Wenping Sun, Ben Xu, Mi Yan

PII: S2211-2855(14)00010-X
DOI: http://dx.doi.org/10.1016/j.nanoen.2014.02.002
Reference: NANOEN324

To appear in: *Nano Energy*

Received date: 10 December 2013
Revised date: 31 January 2014
Accepted date: 4 February 2014

Cite this article as: Yinzhu Jiang, Meijuan Hu, Dan Zhang, Tianzhi Yuan, Wenping Sun, Ben Xu, Mi Yan, Transition metal oxides for high performance sodium ion battery anodes, *Nano Energy,* http://dx.doi.org/10.1016/j.nanoen.2014.02.002

Transition metal oxides for high performance sodium ion battery anodes

Yinzhu Jiang [a,], Meijuan Hu [a], Dan Zhang [a], Tianzhi Yuan [a], Wenping Sun [b], Ben Xu [c], Mi Yan [a,*]*

[a] *State Key Laboratory of Silicon Materials, Key Laboratory of Advanced Materials and Applications for Batteries of Zhejiang Province, Department of Materials Science and Engineering, Zhejiang University, Hangzhou 310027, China*

[b] *CAS Key Laboratory of Materials for Energy Conversion, Department of Materials Science and Engineering, University of Science and Technology of China, Hefei, 230026, China,*

[c] *Laboratory of Smart Materials and Surface, Mechanical Engineering, Faculty of Engineering and Environment, Northumbria University, Newcastle, NE1 8st, UK*

*Correspondence authors: yzjiang@zju.edu.cn (Y.Z. Jiang); mse_yanmi@zju.edu.cn (M. Yan)

Abstract

Sodium-ion batteries (SIBs) are attracting considerable attention with expectation of replacing lithium-ion batteries (LIBs) in large-scale energy storage systems (ESSs). To explore high performance anode materials for SIBs is highly desired subject to the current anode research mainly limited to carbonaceous materials. In this study, a series of transition metal oxides (TMOs) is successfully demonstrated as anodes for

SIBs for the first time. The sodium uptake/extract is confirmed in the way of reversible conversion reaction. The pseudocapacitance-type behavior is also observed in the contribution of sodium capacity. For Fe_2O_3anode, a reversible capacity of 386 mAh g^{-1}at 100 mA g^{-1} is achieved over 200 cycles; as high as 233 $mAhg^{-1}$is sustained even cycling at a large current-density of 5 A g^{-1}.

Keywords: Sodium ion battery; Anode; Transition metal oxide; Conversion reaction.

1. Introduction

Renewable clean energy technologies are important to address global concerns regarding depletion of fossil-based resources, global warming and environmental pollution. However, the widespread implementation of the renewable energy is seriously hampered by the intermittent nature of geographic and climatic environment. Energy storage plays a crucial role in succeeding for renewable energy integration [1-5]. Among the various available energy storage technologies, lithium-ion batteries (LIBs), being used as power sources of portable electronics for decades, are currently considered as the dominant candidate to power the next generation of electric vehicles and stationary applications. Unfortunately, the large-scale commercial manufacturing of LIBs faces severe challenges from the increasing cost of lithium and the limited size of reserves (0.006 wt% abundance on earth) [6,7]. On the other hand, there is no doubt that the sodium resources are inexhaustible and unlimited everywhere around the world (4^{th} most abundant element, 2.64 wt% on earth). Similar to LIBs, sodium-ion batteries (SIBs) could provide an alternative chemistry and might thus

become economically more competitive especially in large-scale energy storage systems (ESSs) [8-11]. Most SIB research were focused on exploration of stable and low-cost cathode materials, including Prussian blue, $NaFePO_4$ and $NaNi_{0.5}Mn_{0.5}O_2$ [12-14]. There are continuous efforts on exploring the anode material, most of which, limited in nongraphitic carbonaceous materials. Hard carbon is the top ranked nongraphitic carbonaceous materials for sodium storage due to the large interlayer distance and the disorder structure [8]. Stevens and Dahn reported an initial reversible capacity of hard carbon as high as 300 mAh g^{-1} [15]. However, some disadvantages are revealed for non-graphitic carbonaceous materials such as the large irreversible capacity and poor capacity retention [14-17]. Some approaches on Na-alloying metals such as Sn and Sb based materials were also confirmed with sodium storage capability [18-23]. The SnSb/C nanocomposites exhibited 435 mAh g^{-1} at 100 mA g^{-1} after 50 cycles; also, a capacity of 274 mAh g^{-1} was sustained when applying a large current density of 1000 mA g^{-1} [19]. Monconduit *et al.* reported a good cycling performance of bulk Sb (600 mAh g^{-1} at C/2 after 100 cycles) subject to the amorphous intermediate phase Na_xSb acting as a buffer to relieve strain [20].

The conversion-type materials (*eg.* transition metal oxides, TMO), with superior lithium storage properties, are also proposed to act as anodes for SIBs. The concept was first demonstrated with the spinel $NiCo_2O_4$ which delivered ~200 mAh $g^{-1}$of reversible capacity after an initial discharge of 618 mAh g^{-1} [24]. Balaya *et al.* investigated the sodium storage of Fe_3O_4 anode, which exhibited an initial discharge of 643 mAh g^{-1} but accompanied with nearly 50% irreversible capacity and very poor

capacity retention [25]. Recently, α-MoO_3 was demonstrated with highly electrochemical activity for sodium storage, delivering high first cycle sodiation and desodiation capacities of 771 and 410 mAh g^{-1} respectively. Moreover, the α-MoO_3 anodes showed favorable rate performance 100 mAh g^{-1} at a current density of 1.117 A g^{-1} and long durability over 500 cycles [26]. K. Edstr□m *et. al* examined nanostructured Fe_2O_3 for both lithium and sodium storage. A specific sodium capacity of 250 mAh g^{-1} at 130 mA g^{-1} was attained after 60 cycles [27]. However, there are also contradictory reports that transition metal oxides such as FeO, CoO and NiO showed almost no electrochemical activity with Na-ion [18,28,29]. In all, there are limited investigation on using TMOs SIB anode and the mechanism remains poorly understood.

In this paper, we develop a series of TMOs including Fe_2O_3, NiO, Co_3O_4 and Mn_3O_4 thin films as anodes of SIBs. The results show high electrochemical activities of all these TMOs in SIBs. Especially for Fe_2O_3, as high as 386 mAh g^{-1}capacity at 100 mAg^{-1}could be sustained after 200 cycles. More surprisingly, a reversible capacity of 233 mAh g^{-1} is achieved even at an ultra-large current density of 5,000 mA g^{-1}, which is one of the best rate performances among all SIB anodes ever reported. Further investigation clearly indicates that both the traditional conversion reactions and the pseudocapacitance-type behavior contribute the distinguished sodium storage performance. This work demonstrates that TMO based materialsmay actas a suitable candidateforward to develop high performance anodes of SIBs.

2. Experimental section

Preparation of transition metal oxide film: With a precursor solution of 0.005 M ferric nitrate in ethanol and ethylene glycol (4:1 in volume), porous Fe_2O_3 thin films were prepared by electrostatic spray deposition (ESD) technique for 3h on a stainless steel substrate heated at 180°C (feeding rate:2 mL h^{-1}). The distance and the applied voltage between the nozzle and substrate were 4 cm and 15kV, respectively. The mass of the deposited material was measured using a microbalance with an accuracy of 0.002mg (Sartorius CPA26P, Germany) before and after deposition. The deposition conditions of NiO, Co_3O_4 and Mn_3O_4 thin films are listed in Table S1, the other unlisted conditions remained same as Fe_2O_3.

Characterization: The crystal structure of the film was characterized with a Rigaku D/max 2550PC X-ray diffractometer (XRD). The morphology of the film was observed using scanning electron microscopy (SEM; Hitachi S-4800, Tokyo, Japan). The crystal structure details were further characterized by transmission electron microscopy (TEM; CM-200 microscope, PHILIPS, Amsterdam, the Netherlands). X-ray photoelectron spectroscopic (XPS) measurements were performed with an ESCALAB 250 X-ray photoelectron spectrometer, using excitation energy of 1486.6 eV (Al Kα).

Electrochemical Measurements: The electrochemical behavior was examined in CR2025 coin-type cells using the as-deposited films on stainless steel substrate as the working electrode and sodium foil as the counter and reference electrode, respectively. Cell assembling was carried out in an argon filled glovebox, in which the oxygen

concentration and moisture level were maintained less than 1 ppm. Celgard 2300 microporous polypropylene was used as a separator. The electrolyte was 1 M $NaPF_6$ in a mixture solvent of ethylene carbonate (EC), diethyl carbonate (DEC) and propylene carbonate (PC) (4:4:2 by volume). The cells were charged and discharged galvanostatically on a Neware BTS battery cycler at 0.005-3.0 V (vs Na/Na^+). Cyclic voltammetry (CV) tests were conducted on a CHI660C electrochemistry workstation between 0.005 and 3.0 V (vs Na/Na^+) at 0.1 mV s^{-1}. All the electrochemical measurements were carried out at room temperature.

3. Results and discussion

Four transitional metal oxide films prepared by ESD technique were identified as crystalline for Co_3O_4, Mn_3O_4 and amorphous for Fe_2O_3 and NiO by the XRD analysis (Figure S1). XPS results of the as-prepared samples verify the valence state of the transition metals (Figure S2). The morphology and cycling performance of Fe_2O_3, NiO, Co_3O_4 and Mn_3O_4 thin films are shown in **Figure 1**. The amorphous Fe_2O_3 film deposited at 180 °C shows a porous 3D reticular structure with ~500 nm-thickness grids cross-linked together (**Figure 1a**). Such a reticular architecture ensures a good wetting of the electrolyte, accommodates the volume changes along with the discharge/charge reactions, and facilitates the fast diffusion of Na-ions as well. Mn_3O_4 thin film exhibits a similar structure as that in Fe_2O_3 film, with larger pores between straighter grids (**Figure 1c**). There are also some minor cracks in the grids, which might be harmful for the structure integration during cycling. In contrast to the reticular structure of Fe_2O_3 and Mn_3O_4, Co_3O_4 film displays a different morphology,

with ~100 nm-diameter nanospheres distributed among cross-linked nanowires. Besides, a few scattered nanoclusters can also be observed on the film (**Figure 1e**). As for the NiO film, the morphology has transferred to the agglomeration of spherical-like grains. (**Figure 1g**).

The electrochemical activity on Na-ion and cycling stability of the four TMO films were evaluated at a constant current density of 100 mA g^{-1}under galvanostatic conditions. All the TMO film anodes considerably delivered the first discharge capacities of 949 (Fe_2O_3), 257 (Mn_3O_4), 582 (Co_3O_4) and 744 mAh g^{-1} (NiO), respectively. The Fe_2O_3 anode exhibits excellent cycling performance, with a reversible capacity as high as 385 $mAhg^{-1}$after 200 cycles, corresponding to 73% capacity retention (**Figure 1b**). Similar to the Fe_2O_3 anode, the Mn_3O_4 film also shows superior stability upon cycling, with 61% initial charge capacity over 200 cycles (**Figure 1d**). In contrast, the capacity decays continuously upon cycling either in Co_3O_4 or NiO (**Figure 1f** and **h**). As stated, the reticular structure in both the Fe_2O_3 and Mn_3O_4 films might be beneficial for the relief of volume change and thus keep the electrode integration during cycling, leading to a superior cycling performance compared with Co_3O_4 and NiO.

For conversion-type anodes, a high potential hysteresis is observed due to the energy penalty associated with the formation of nanoparticles in LIBs. Figure S3 presents the voltage profiles of the first two discharge/charge curves for the four TMO anodes applying a current density of 100 mA g^{-1}. It is found that the voltage hysteresis of Fe_2O_3 and Co_3O_4 is roughly 0.75-1.0 V and 0.86 V between the characteristic

red-ox plateaus respectively, while a higher voltage hysteresis of NiO (1.12 V) and Mn_3O_4 (1.30 V) is recorded, suggesting a faster sodium reaction kinetics for Fe_2O_3 and Co_3O_4 electrodes. To further explore the electrochemical behavior along with Na-ion uptake/extraction, cyclic voltammetry (CV) was applied for the evaluation of the Fe_2O_3anode, as shown in **Figure 2a**. The charge-discharge curves of the Fe_2O_3anode are also included for comparison. During the first sodiation process, a strong peak at 0.54 V is clearly observed. Correspondingly in the voltage profiles (**Figure 2b**), a long plateau in the range of 0.9-0.6 V is also found. Considering the fact that the galvanostatic battery test and CV can't be operated in the exact same condition, there might probably be a little variation between the peak position of CV and the plateau range of voltage profile. Nevertheless, it can be concluded that the strong peak at 0.54 V corresponds to the long plateau discharge, which might be attributed to the reduction of Fe (III) to Fe (0). Additionally, in the second discharge process, the reduction peak centered at 0.54 V has shifted to 0.65 V with an obvious intensity drop, due to the decomposition of the liquid electrolyte and formation of an SEI layer in the first cycle.

On the other hand, we have previously investigated the electrochemical behavior of Fe_2O_3 electrode in LIBs system. The CV curves and voltage profiles of Fe_2O_3 in LIBs are presented (Figure S5) in order to investigate the difference of electrochemical behavior between SIBs and LIBs [30]. In the first lithiation process, there are two clear peaks at 1.3 V and 0.72 V in accordance with the two plateaus in the voltage profiles, indicating Li inserting into amorphous Fe_2O_3 and reduction of Fe (III) to Fe (0),

respectively. In the case of SIBs, only the last reaction occurred. Besides, the reduction peak of Fe_2O_3 in SIBs is lower than in LIBs, which would provide a higher output voltage and power density when applied in the full cell.

In the research of TMO based anodes for LIBs, there is a general understanding of that the capacity is partly contributed from pseudocapacitance behavior as signaled by the sloping curve that follows the conversion plateau in the discharge curve. In our case of SIBs, a similar long sloping tail until the termination of discharge is also seen (**Figure 2b**). To investigate the whether such pseudocapacitance-type behavior of TMO based anodes exists in SIBs as well, a series CV curves at scan rates of 0.1-6 mV s^{-1} was measured for the Fe_2O_3 anode (**Figure 2c**). Upon increasing the scanning rate, the current increases and the redox peaks vanishes gradually, finally leading to a mirror-like-image shape, which is usually considered as a signature mark for capacitance/pseudocapacitance-type behavior. From the liner relationship between the current and scan rate (**Figure 2**d), we can extract a capacitance of ~572 F g^{-1} according to C=I/(dV/dt) g^{-1} [31,32]. Considering the limited electrical double-layer capacitance, such a large value of capacitance further provides an affirmative evidence of pseudocapacitance-type behavior, which might be caused by catalytically enhanced electrolyte decomposition [31]. Based on the analysis above, we can conclude that the pseudocapacitance-type behavior of TMO based electrodes also contributes for the sodium storage, as characterized by the sloping tail in the discharge profile and ~0.21 V broad peak in the CV curve.

The morphological and compositional changes of the Fe_2O_3 film after discharge and charge process are shown in **Figure 3**. After the complete discharge on 0.005V, the initial reticular structure can't be observed (**Figure 3a**), replaced by the crossed nanoplates dispersing in the porous matrix of nanoparticles. The corresponding SAED pattern (**Figure 3b**) shows diffraction spots/rings that are characteristic of three phases including Na_2O, metallic Fe and Fe_2O_3, indicating the occurrence of conversion reaction during sodiation. The results show consistency with that of XPS investigation (Figure S4). As shown in **Figure 3a**, the newly generated nanoplates might be metallic Fe, surrounded by Na_2O nanoparticles matrix. Besides, the presence of a small quantity of Fe_2O_3 phase was caused by the oxidization of Fe in the air atmosphere and/or incomplete reduction during Na insertion. When recharging back to 3.0 V, the porous 3D reticular structure returned back as well as a fresh film (**Figure 3c**), except for a few minor cracks observed. The SAED pattern also confirms the complete oxidation of metallic Fe by the fact of only Fe_2O_3 phase indexable. The residual Na_2O phase might be caused by electrolyte decomposition, which has also been confirmed in the previous report of α-MoO_3 [26]. The SAED investigation and above CV analysis clearly suggest the conversion reaction as follows:

$$Fe_2O_3+6Na^++6e^-\leftrightarrow 2Fe^0+3Na_2O$$

In addition to the high reversible capacity and excellent capacity retention, the Fe_2O_3 electrodes also display outstanding high rate capability (**Figure 4a**). The Fe_2O_3 electrode delivers specific capacities of 610, 561, 474, 418, 371 and 323 mAh g^{-1} at current densities of 0.05, 0.1, 0.2, 0.5, 1.0 and 2.0 A g^{-1} respectively. Even cycled at an

ultra-large current density of 5.0 A g^{-1}, a record capacity of 233 mAh g^{-1}could still be sustained, which exceeds most SIB anodes previously reported including nongraphitic carbon and Na-alloy metals [15-26]. After cycling at high rates, a specific capacity as high as 604 mAh g^{-1}can be recovered when the current density is reduced back to 0.05 A g^{-1}. Worthy of noting is that the anomalous Coulombic efficiency is observed at low current density (50-100 mA g^{-1}), which might be avoided by switching appropriate electrolyte [33]. Furthermore, we also evaluated the long-term cycling performance of the Fe_2O_3 anode at high current densities (**Figure 4b**). Interestingly, there are minor capacity drops with the increase of the current density and the capacity kept rather high and stable even after 200 cycles: 386 mAh g^{-1}at 100 mA g^{-1}, 331 mAhg^{-1} at 200 mA g^{-1} and 273 mAhg^{-1} at 1000 mA g^{-1}. The pseudocapacitance-type behavior might play a key role in the superior rate capability of TMO anodes, which inspires the potential power application of SIBs in the future.

4. Conclusions

In summary, we have fabricated series of transition metal oxides including Fe_2O_3, Mn_3O_4, Co_3O_4 and NiO, and characterized the relative electrochemical properties with application of anodes for SIBs. The sodium uptake/extract was confirmed in the way of reversible conversion reaction. The pseudocapacitance-type behavior was also observed in the contribution of sodium capacity as that in previous reports on LIBs. A large reversible capacity of 386 mAh g^{-1}at 100 mA g^{-1} was maintained over 200 cycles; meanwhile, a high capacity of 233 mAh g^{-1} has been sustained even cycling at a large current-density of 5 A g^{-1}. The high reversible capacity, excellent cycling

stability and superior rate capability of the TMO electrode offer great potential forward to develop high-performance SIB anodes reacting through conversion reactions.

Acknowledgements

This work was supported by National Natural Science Foundation of China (NSFC-21373184) and Doctoral Fund of Ministry of Education of China. Dr. Yinzhu Jiang wishes to acknowledge an equipment subsidy offered by Alexander von Humboldt (AvH) Foundation.

References

[1] M.E. Mann, R.S. Bradley, M.K. Hughes, *Nature* **1998**, 392, 779-787.

[2] K. Tomabechi, *Energies* **2010**, 3, 686-695.

[3] M. Winter, R.J. Brodd, *Chem. Rev.* **2004**, 104, 4245-4269.

[4] C.J. Barnhart, S.M. Benson, *Energy Environ. Sci.* **2013**, 6, 1083-1092.

[5] A.L.M. Reddy, S.R. Gowda, M.M. Shaijumon, P.M. Ajayan, *Adv. Mater.* **2012**, 24, 5045.

[6] B. Kang, G. Ceder, *Nature* **2009**, 458, 190-193.

[7] B. Scrosati, J. Hassoun, Y.K. Sun, *Energy Environ. Sci.* **2011**, 4, 3287-3295.

[8] M.D. Slater, D. Kim, E. Lee, C.S. Johnson, *Adv. Funct. Mater.* **2013**, 23, 947-958.

[9] V. Palomares, P. Serras, I. Villaluenga, K.B. Hueso, J. Carretero-Gonzalez, T. Rojo, *Energy Environ. Sci.* **2012**, 5, 5884-5901.

[10] S.P. Ong, V.L. Chevrier, G. Hautier, A. Jain, C. Moore, S. Kim, X.H. Ma, G. Ceder, *Energy Environ. Sci.* **2011**, 4, 3680-3688.

[11] S.W. Kim, D.H. Seo, X.H. Ma, G. Ceder, K. Kang, *Adv. Energy Mater.* **2012**, 2, 710-721.

[12] Y.H. Lu, L. Wang, J.G. Cheng, J.B. Goodenough, *Chem. Commun.* **2012**, 48, 6544–6546.

[13] S.M. Oh, S.T. Myung, J. Hassoun, B. Scrosati, Y.K. Sun, *Electrochem. Commun.* **2012**, 22, 149-152.

[14] S. Komaba, W. Murata, T. Ishikawa, N. Yabuuchi, T. Ozeki, T. Nakayama, A. Ogata, K. Gotoh, K. Fujiwara, *Adv. Funct. Mater.* **2011**, 21, 3859-3867.

[15] D.A. Stevens, J.R. Dahn, *J. Electrochem. Soc.* **2000**, 147, 1271-1273.

[16] K. Tang, L.J. Fu, R.J. White, L.H. Yu, M.M. Titirici, M. Antonietti, J. Maier, *Adv. Energy Mater.* **2012**, 2, 873-877.

[17] Y. Cao, L. Xiao, M.L. Sushko, W. Wang, B. Schwenzer, J. Xiao, Z. Nie, L.V. Saraf, Z. Yang, J. Liu, *Nano Lett.* **2012**, 12, 3783-3787.

[18] Q. Sun, Q.Q. Ren, H. Li, Z.W. Fu, *Electrochem. Commun.* **2011**, 13, 1462-1464.

[19] L.F. Xiao, Y.L. Cao, J. Xiao, W. Wang, L. Kovarik, Z.M. Nie, J. Liu, *Chem. Commun.* 2012, 48, 3321-3323.

[20] A. Darwiche, C. Marino, M.T. Sougrati, B. Fraisse, L. Stievano, L. Monconduit, *J. Am. Chem. Soc.* **2012**, 134, 20805-20811.

[21] Y.H. Liu, Y.H. Xu, Y.J. Zhu, J.N. Culver, C.A. Lundgren, K. Xu, C.S. Wang, *ACS Nano* **2013**, 7, 3627-3634.

[22] D.W. Su, H.J. Ahn, G.X. Wang, *Chem. Commun.* **2013**, 49, 3131-3133.

[23] L. Wu, P. Pei, R.J. Mao, F.Y. Wu, Y. Wu, J.F. Qian, Y.L. Cao, X.P. Ai, H.X. Yang, *Electrochim. Acta* **2013**, 87, 41-45.

[24] R. Alcantara, M. Jaraba, P. Lavela, J.L. Tirado, *Chem. Mater.* **2002**, 14, 2847-2848.

[25] S. Hariharan, K. Saravanan, V. Ramar, P. Balaya, *Phys. Chem. Chem. Phys.* **2013**, 15, 2945-2953.

[26] S. Hariharan, K. Saravanan, P. Balaya, *Electrochem. Commun.* **2013**, 31, 5-9.

[27] M. Valvo, F. Lindgren, U. Lafont, F. Bj□refors, K. Edstr□m, *J. Power Sources* **2014**, 245, 967-978.

[28] H. Kim, D.-H. Seo, S.-W. Kim, J. Kim , K. Kang , *Carbon* **2011**, 49, 326.

[29] S.-W. Kim, D.-H. Seo, X.H. Ma, G. Ceder, K. Kang, *Adv. Energy Mater.* **2012**, 2, 710-721.

[30] Y.Z. Jiang, D. Zhang, Y. Li, T.Z. Yuan, N. Bahlawane, C. Liang, W.P. Sun, Y.H. Lu, M. Yan, *Nano Energy* **2014**, 4, 23-30.

[31] S. Laruelle, S. Grugeon, P. Poizot, M. Dolle, L. Dupont, J.M. Tarascon, *J. Electrochem. Soc.* **2002**, 149, A627-A634.

[32] R. Ding, L. Qi, M. Jia, H. Wang, *Electrochim. Acta* **2013**, 107, 494-502.

[33] B. Koo, S. Chattopadhyay, T. Shibata, V.B. Prakapenka, C.S. Johnson, T. Rajh, E.V. Shevchenko, *Chem. Mater.* **2013**, 25, 245-252.

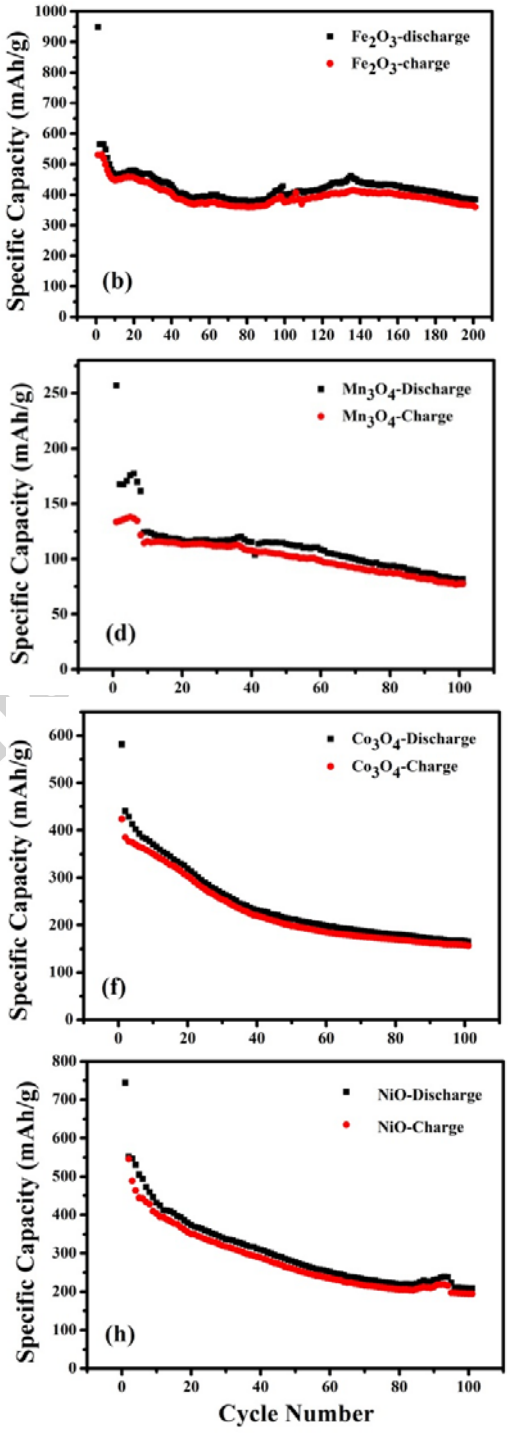

Figure 1 SEM images of the as-prepared Fe_2O_3 (a), Mn_3O_4 (c), Co_3O_4 (e), NiO (g) film, cycle performance of Fe_2O_3 (b), Mn_3O_4 (d), Co_3O_4 (f), NiO (h) at current density of 100 mA g^{-1}.

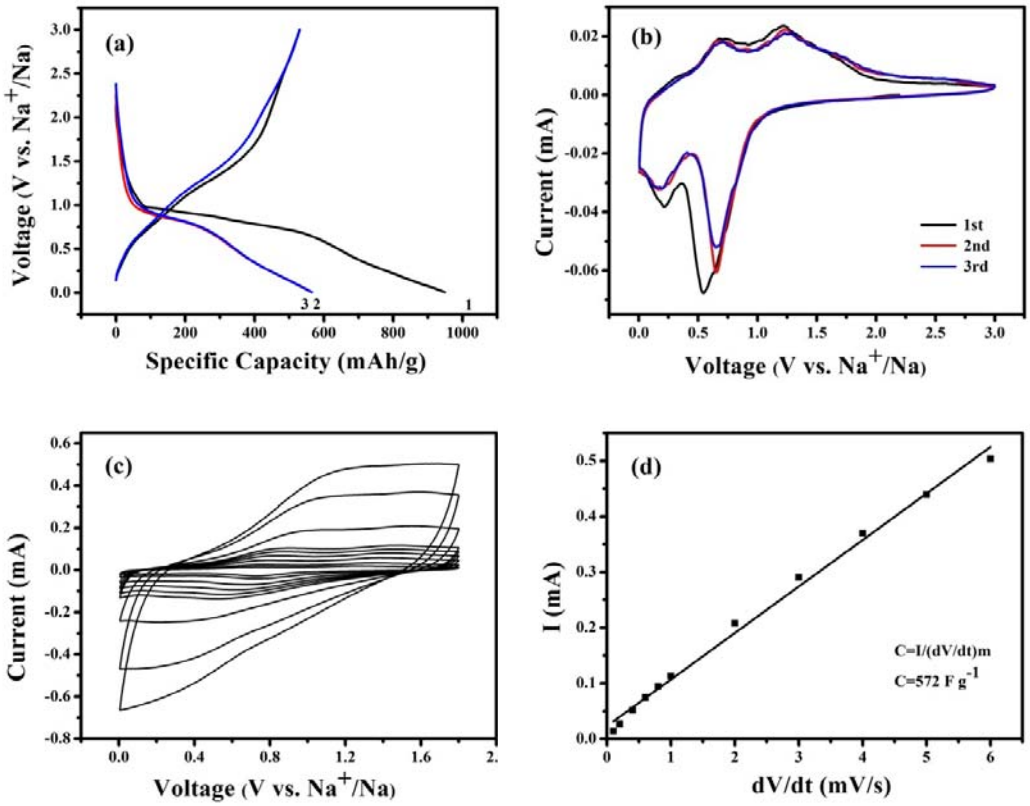

Figure 2 (a) The 1st, 2nd and 3th charge–discharge curve of Fe_2O_3, (b) CV curves of Fe_2O_3 composite electrode at a scan rate of 0.1 mV s^{-1} for the first three cycles within a potential range of 0.005 to 3.0 V (vs. Na/Na^+), (c) CV curves for a Fe_2O_3/Na cell that was initially discharged down to 0.005V. The cell was cycled between 0.005 and 1.8 V at scanning rates varying form 0.1 to 6 mV s^{-1}, (d) The linear variation of the current (taken as constant over 1.6 to 1.8 V voltage ranges) as a function of the scan rate.

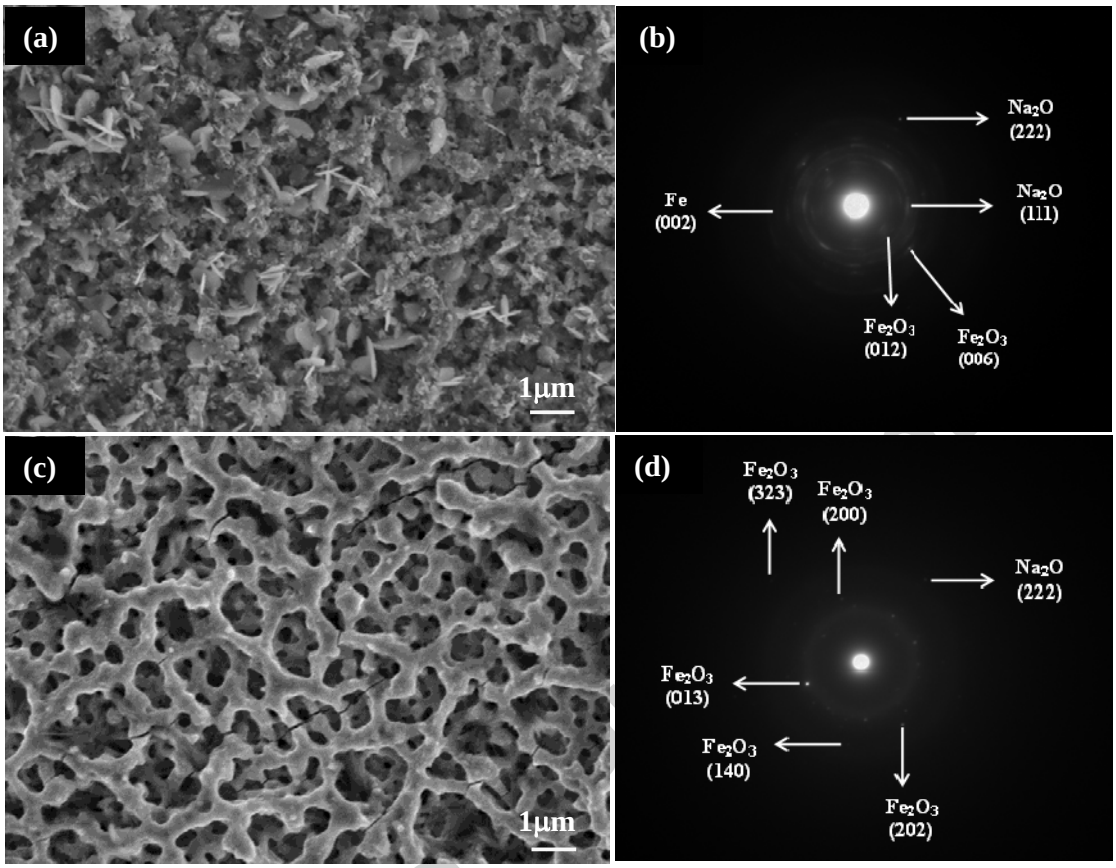

Figure 3 SEM image and SAED patterns of Fe_2O_3 electrode after (a and b) first discharge to 0.005 V vs. Na/Na^+ and (c and d) first charge to 3.0 V.

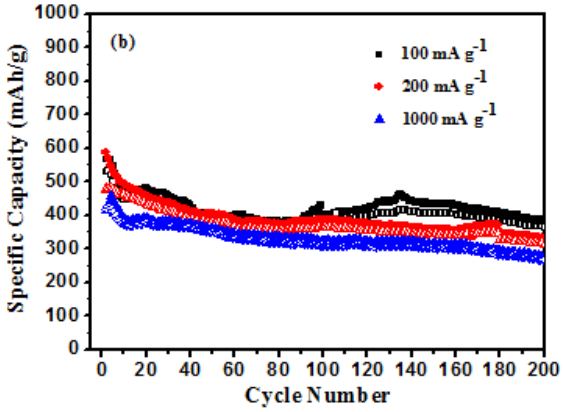

Figure 4 Rate performances (a) and cycling performance (b) at different current densities of 100, 200 and 1000 mA g^{-1}.

Highlights:

1. A series of transition metal oxides is successfully demonstrated as anodes for sodium ion batteries.
2. The sodium uptake/extract is confirmed in the way of reversible conversion reaction.
3. The pseudocapacitance-type behavior is observed in the contribution of sodium capacity.
4. For Fe_2O_3 anode, a reversible capacity of 386 mA h g^{-1} at 100 mA g^{-1} is achieved over 200 cycles;
5. As high as 233 mA h g^{-1} is sustained even cycling at a large current-density of 5 A g^{-1}.

TOC graphic:

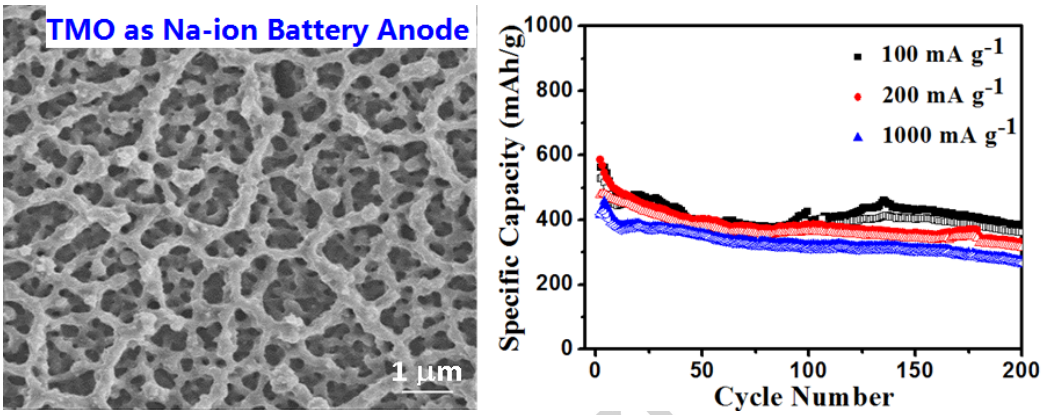

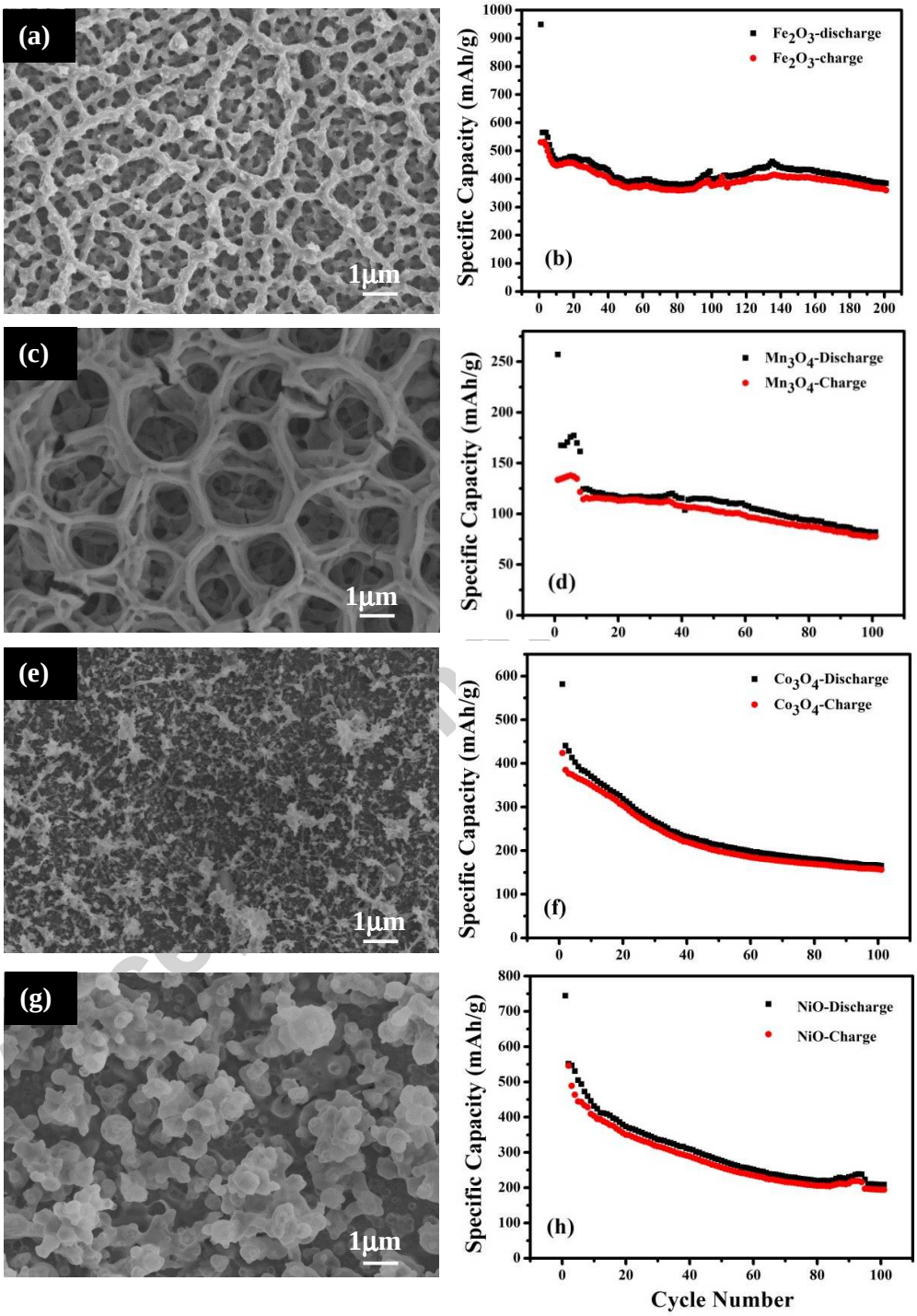

Figure 1 SEM images of the as-prepared Fe_2O_3 (a), Mn_3O_4 (c), Co_3O_4 (e), NiO (g) film, cycle performance of Fe_2O_3 (b), Mn_3O_4 (d), Co_3O_4 (f), NiO (h) at current density of 100 mA g^{-1}.

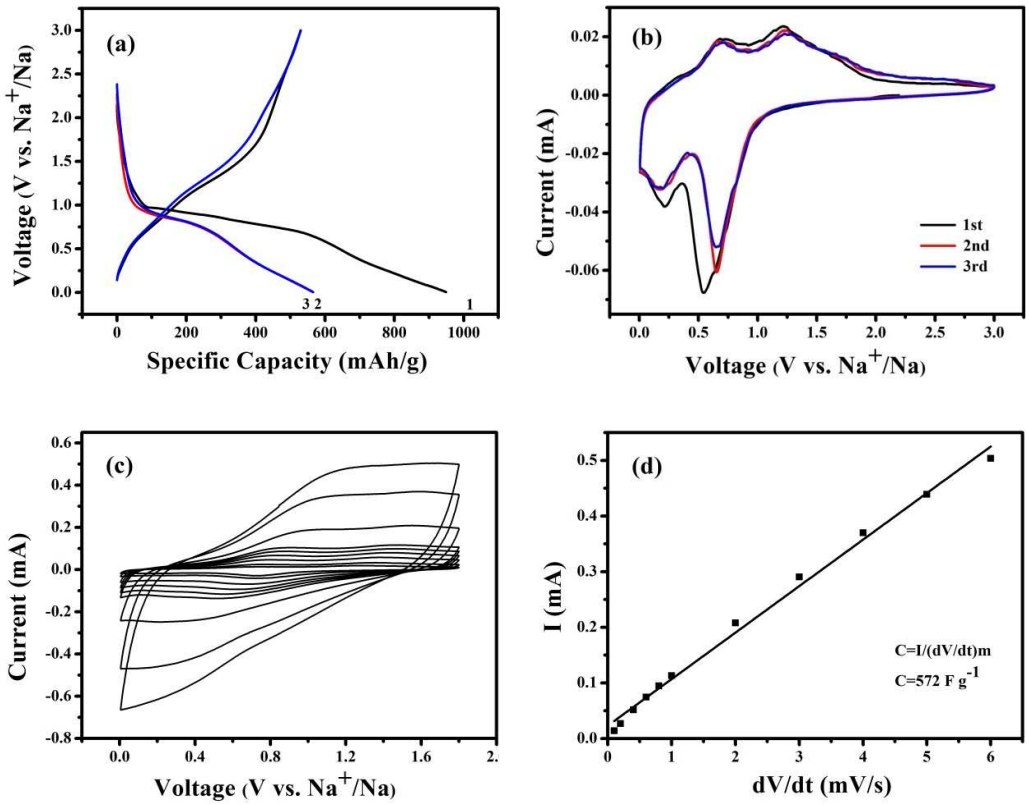

Figure 2 (a) The 1st, 2nd and 3th charge–discharge curve of Fe_2O_3, (b) CV curves of Fe_2O_3 composite electrode at a scan rate of 0.1 mV s^{-1} for the first three cycles within a potential range of 0.005 to 3.0 V (vs. Na/Na^+), (c) CV curves for a Fe_2O_3/Na cell that was initially discharged down to 0.005V. The cell was cycled between 0.005 and 1.8 V at scanning rates varying form 0.1 to 6 mV s^{-1}, (d) The linear variation of the current (taken as constant over 1.6 to 1.8 V voltage ranges) as a function of the scan rate.

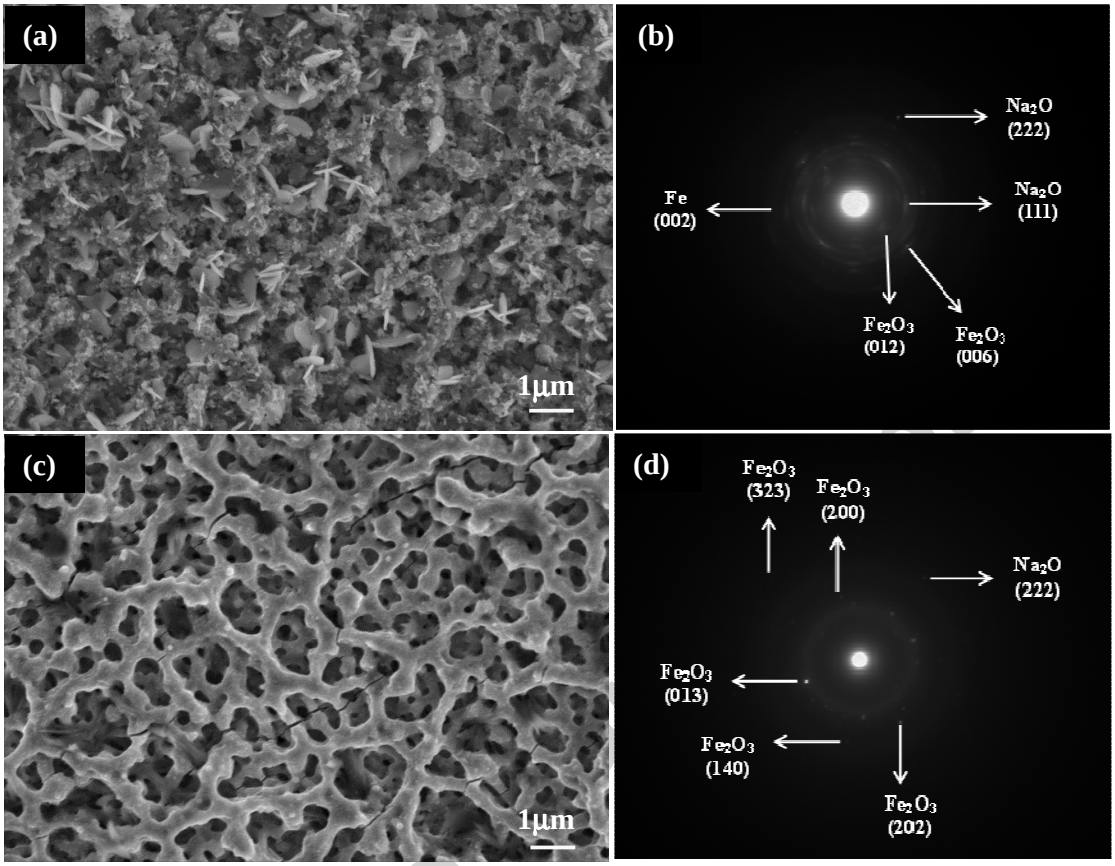

Figure 3 SEM image and SAED patterns of Fe_2O_3 electrode after (a and b) first discharge to 0.005 V vs. Na/Na^+ and (c and d) first charge to 3.0 V.

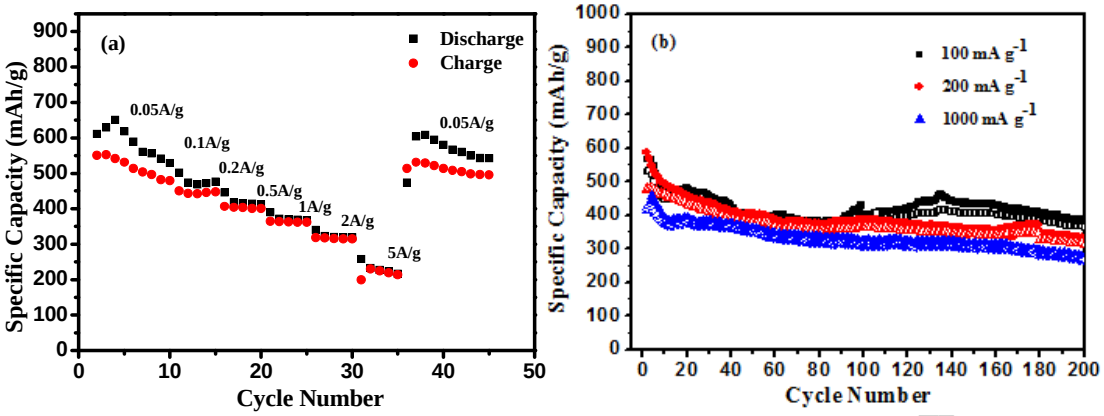

Figure 4 Rate performances (a) and cycling performance (b) at different current densities of 100, 200 and 1000 mA g^{-1}.

*Graphical Abstract

TOC graphic: